Impact Generation of Holes in the Early Lunar Crust I: Scaling Relations

Jackson Alan Patrick[1], Perera Viranga[2], and Gabriel Travis S. J.[3]

[1]Arizona State University
[2]The University of Texas at Austin
[3]U.S. Geological Survey Astrogeology Science Center

November 16, 2022

Abstract

After its formation, the Moon is widely believed to have possessed a deep, global magma ocean. As it cooled, an anorthositic crust formed, floating atop this magma ocean, and acting as an insulating blanket. As well as forming the Moon, the Moon-forming giant impact also released more than a lunar mass of debris into heliocentric orbit. Re-impacting debris subjected the newly formed Moon to an extremely intense bombardment. We have conducted a suite of impact simulations for a range of conditions representative of this early period. We find that impact outcomes can be divided into four regimes, and construct scaling relations for the transitions between these regimes and size of impact features. Exposure of liquid magma to the surface is generally more efficient than previously assumed, implying significant shortening of the solidification time of the Lunar Magma Ocean. Comparison with work on icy satellites also suggests that penetration of a solid crust overlying liquid is a relatively universal process with weak dependence on target material properties.

Impact Generation of Holes in the Early Lunar Crust I: Scaling Relations

Alan P. Jackson[1,2*], **Viranga Perera**[3†], **Travis S.J. Gabriel**[1]

[1]School of Earth and Space Exploration, Arizona State University, 781 E Terrace Mall, Tempe, AZ 85287, USA
[2]Centre for Planetary Sciences, University of Toronto, 1265 Military Trail, Toronto, Ontario, M1C 1A4, Canada
[3]Physics Department, The University of Texas at Austin, 2515 Speedway, C1600, Austin, TX 78712, USA.

Key Points:

- Impacts into crusts overlying magma can be divided into four outcomes ranging from classical crater-forming to complete penetration
- We derived impact energy scaling relations for the transitions between regimes and size of impact features
- Penetration of the early lunar crust would have been extensive – re-impacting debris is important for Lunar Magma Ocean solidification

*ORCID: 0000-0003-4393-9520
†0000-0002-6061-4915

Corresponding author: Alan P. Jackson, `alan.jackson@asu.edu`

Abstract

After its formation, the Moon is widely believed to have possessed a deep, global magma ocean. As it cooled, an anorthositic crust formed, floating atop this magma ocean, and acting as an insulating blanket. As well as forming the Moon, the Moon-forming giant impact also released more than a lunar mass of debris into heliocentric orbit. Re-impacting debris subjected the newly formed Moon to an extremely intense bombardment. We have conducted a suite of impact simulations for a range of conditions representative of this early period. We find that impact outcomes can be divided into four regimes, and construct scaling relations for the transitions between these regimes and size of impact features. Exposure of liquid magma to the surface is generally more efficient than previously assumed, implying significant shortening of the solidification time of the Lunar Magma Ocean. Comparison with work on icy satellites also suggests that penetration of a solid crust overlying liquid is a relatively universal process with weak dependence on target material properties.

Plain Language Summary

The Moon is believed to have formed in a giant impact between Earth and another planet-size body. After formation the Moon was very hot and likely had a deep layer of magma. As the magma cooled and solidified, some of the solid minerals floated to the surface, creating an insulating blanket. As well as forming the Moon, the giant impact released over a Moon's mass of debris into orbit around the Sun, some of which returned to hit the young Moon. We ran computer simulations to understand what happens to the solid crust when debris hits it. We find that these impacts can be divided into four types and developed equations relating the size of the scar produced to impact energy and crust thickness. Creating a hole in the crust makes it a less effective insulating blanket, allowing heat out faster. We find that impacts more easily produce holes than previously assumed, so the magma should have cooled faster. Icy satellites are similar in structure having a solid ice layer with water underneath, and comparing with previous work we suggest that how easy it is to puncture the solid layer does not depend much on what it is made out of.

1 Introduction

The most widely accepted hypothesis for the origin of Earth's Moon is the giant impact hypothesis, in which the young Earth is struck by another planetary-sized body (e.g., Hartmann & Davis, 1975; Cameron & Ward, 1976; Canup, 2004). The Canonical model, developed over several decades, settled on a low velocity, glancing impact between a roughly Mars-sized body (commonly known as 'Theia' after the mother of Selene, goddess of the Moon in Greek mythology) and the proto-Earth in the late stages of its formation (see Canup, 2004, for a review). The Canonical model readily explains the high ratio of angular momentum in the lunar orbit relative to the whole Earth-Moon system, and the depletion of the Moon in iron and volatile elements relative to Earth (Taylor et al., 2006). More recently, doubts have been cast on the Canonical model as a result of geochemical analyses that have revealed the Moon to have nearly identical isotopic signatures to Earth (e.g., Spicuzza et al., 2007; Zhang et al., 2012), which conflicts with the prediction of the Canonical model that lunar material should be predominantly sourced from Theia (e.g., Canup, 2014). This has led to a number of proposals for modified giant impact scenarios (e.g., Ćuk & Stewart, 2012; Canup, 2012; Reufer et al., 2012; Rufu et al., 2017), but the basic premise of a giant impact origin for the Moon remains by far the most widely accepted (Asphaug, 2014; Barr, 2016).

All giant impact models of Moon formation produce a liquid-vapour disk in orbit around Earth from which the Moon forms. However, a sizeable amount of unbound debris is also produced in giant impacts, which enters heliocentric orbit and can reimpact the remnant some time later (e.g., Benz et al., 1988; Leinhardt & Richardson, 2005; Jackson & Wyatt, 2012). Indeed, production of debris is a generic property of all giant impacts (e.g., Agnor

& Asphaug, 2004; Leinhardt & Stewart, 2012; Gabriel et al., 2020). Given that almost all modified giant impact proposals involve greater impact energies than the original Canonical model, it can be expected that they would lead to a substantial amount of escaping debris.

Once in heliocentric orbit the debris naturally becomes a source of impactors for the young Earth and Moon, as well as the rest of the terrestrial planets. Jackson & Wyatt (2012) showed that the bulk of the impacts from this debris population will occur over the first 10-100 Myr after the initial Moon-forming event. This time frame is concurrent with the period in which the Moon is hypothesized to feature a global magma ocean ($\sim$10-250 Myr after formation) (e.g., Wood et al., 1970; Solomon & Longhi, 1977; Nyquist et al., 1995; Rankenburg et al., 2006; Elkins-Tanton et al., 2011). A peculiarity of the Moon is that fractional solidification of the Lunar Magma Ocean (LMO) leads to formation of an anorthositic flotation crust (e.g., Wood et al., 1970; Solomon & Longhi, 1977; Elkins-Tanton, 2012). As such the majority of this returning debris would have struck a layer of solid crust overlying liquid magma, potentially punching holes through the lid and exposing the magma beneath; a considerable deviation from classical cratering where the substrate is entirely solid. Impacts into the ice shell of Europa (e.g., Bauer & Cox, 2011; Bray et al., 2014; Cox & Bauer, 2015) and Enceladus (e.g., Monteux et al., 2016) are perhaps the only modern-day analogues for this phenomenon.

The anorthositic flotation crust plays an important role in insulating the magma ocean and extending the time it takes to solidify (Elkins-Tanton et al., 2011). Perera et al. (2018) (hereafter referred to as P+18) showed that puncturing holes in this insulating lid can decrease the time for LMO solidification by as much as a factor of 6. P+18 did not consider the process of production of individual holes in detail however, instead using simple parametrisations to examine the global influence of holes on the solidification process. Here we instead focus on the phenomenology of puncturing impacts. Our primary interests are in crust morphology after a puncturing impact, how hole size depends on the impact parameters, and what the thresholds are for puncturing the crust. As a secondary consideration we are also interested in how much these impacts fracture the crust since this is the first bombardment of the crust as it is initially forming and thus the first opportunity to fracture the crust on a wide scale.

We outline our numerical methodology in Section 2, both setup of individual simulations (Section 2.1) and the parameter space we explore (Section 2.2). Further details regarding parameter choices, and a discussion of resolution and convergence, are available in the Supplementary Material. In Section 3 we then describe the final morphologies that appear in our suite of simulations, and construct scaling relations for the size of impact features in Section 4. In Section 5 we compare our results with previous work involving ice and water, and with other work on lunar basin formation, and consider implications for the results of P+18. Finally, we summarise our work in Section 6.

2 Hydrocode impact simulations

In this work we use the iSALE-2D hydrocode (Chicxulub and Dellen releases) to simulate the penetration of the early lunar flotation crust by returning debris from the Moon-forming giant impact. The iSALE (*impact* SALE) code is a finite difference shock physics code ultimately based on the SALE (Simplified Arbitrary Lagrangian Eulerian) hydrodynamic solution algorithm (Amsden et al., 1980). It features the ability to simulate collisions in different materials and with different rheologies. To simulate material responses to shocks it includes an elasto-plastic constitutive model as well as fragmentation models and various equations of state (Melosh et al., 1992; Ivanov et al., 1997; Collins et al., 2004). It has been extensively benchmarked, both against other hydrocodes used for modelling impact processes and against laboratory-scale impact experiments (Pierazzo et al., 2008; Miljkovic et al., 2012).

Since we are using a 2D hydrocode we must necessarily make the assumption that the impact direction is exactly vertical and that the impact is cylindrically symmetric. In reality, the most probable impact angle is around 45° to horizontal, with about 50 percent of impacts occurring between 30° and 60° (Shoemaker, 1962) and few occurring very close to vertical or very close to grazing. Studies of the influence of impact obliquity on impact crater morphology have shown that above around 30° the role of obliquity is minor, albeit that it may increase at low impact velocities where the ratio of crater size to impactor diameter is lower (Pierazzo & Melosh, 2000). Elbeshausen et al. (2009) also showed that the influence of obliquity decreases when there is less friction in the target material. Since we are interested in puncturing a solid layer overlying a low viscosity fluid, and broad outcomes rather than detailed morphology, we posit that our vertical impacts will be representative of the majority of impact events. In addition 3D simulations are much more computationally expensive than 2D simulations, and would severely limit the extent of our parameter space exploration.

2.1 Simulation setup

To model the materials in our simulations we use ANEOS equations of state (e.g., Thompson & Lauson, 1974; Thompson, 1990; Melosh, 2007). Impactors and the lunar mantle are represented using ANEOS dunite (Benz et al., 1989), as is commonly the case for impact simulations of the Moon (e.g., Potter et al., 2012; Zhu et al., 2017). The lunar crust is represented using ANEOS granite (Pierazzo et al., 1997), which is also used fairly commonly (e.g. Miljković et al., 2016; Trowbridge et al., 2020). Granite fulfils two key criteria: 1. the crust must have a lower density than liquid dunite (to avoid issues with foundering), and 2. the crust must have a significantly higher melting point than dunite. An ANEOS equation of state for a direct lunar crustal analogue is not available, and the commonly used Tillotson equation of state tuned to gabbroic anorthosite is itself only an approximation, particularly as regards temperature (Potter et al., 2012). The densities of ANEOS granite and lunar anorthosites are similar and Miljković et al. (2016) found that the equation of state has little influence on outcome for large impact events provided that the bulk density is appropriate for lunar crustal material. As such we consider our equation of state implementation to be a reasonable approximation.

The melting point of ANEOS granite, at around 1670 K, is somewhat higher than the $\sim$1500 K of typical Tillotson anorthosite implementations, but the melting point of ANEOS dunite ($\sim$1370 K) is also somewhat higher than estimates for the LMO solidus, which for the prescription used by e.g., P+18 and Elkins-Tanton et al. (2011) drops as low as 1000 K near the end of solidification. Using ANEOS granite thus allows a more realistic temperature differential between the crust melting temperature and the sub-surface magma.

The liquid magma is assumed to be convecting and thus to obey an adiabatic temperature profile, which we also assume extends into solid portions of the mantle below. Surface temperature is held constant at 293 K, accounting for warm post-impact conditions (the blackbody equilibrium temperature at 1 AU is 250 K). The temperature gradient in the crust is adjusted such that the depth of the liquid magma layer (as determined by the point at which the adiabat crosses the dunite solidus) matches the crust thickness according to the results of P+18 and Elkins-Tanton et al. (2011).

We utilise a rock strength model combined with an Ohnaka thermal softening model (Ohnaka, 1995) while damage is computed using the Ivanov et al. (1997) model. Numerically 'damage' serves to transition the material from a higher shear-strength (intact) state to a lower shear-strength (fractured) state. Note that the liquid magma is treated as strengthless and thus registers as completely damaged in the simulation as soon as it is perturbed, but in physical terms there is no difference between damaged and undamaged for a strengthless liquid. Similarly to Potter et al. (2012), we find that strong thermal softening in the crust and the presence of strengthless magma beneath renders acoustic fluidization unnecessary, and so we do not include it.

Further details regarding the rheological and strength models can be found in Supplementary Material S1, while additional information regarding the temperature and yield strength profiles is available in Supplementary Material S2.

2.1.1 Resolution

As in most numerical studies, the resolution of our simulations is a balance between computational demands and achieving the most accurate results possible. The simulation volumes we use here are large compared to most numerical cratering studies. In iSALE the simulation volume consists of a core high-resolution zone in which cells are a constant size, surrounded by extension zones in which cell sizes grow exponentially.

Cell size in the high-resolution zone is set according to several limits. The first of these is that there must always be at least 8 cells across the projectile radius (16 per projectile diameter). The second limit is based on the number of cells across the crust thickness, with the minimum in most cases set at 40 cells, but in some cases (large impactors into thin crust) this resolution would result in well over 10^6 cells in the high resolution zone and infeasibly long run times (many months). In these cases we allow for a coarser resolution that results in at least 10 cells over the crust thickness. Finally, our third limit comes into play for our thickest crusts where the liquid magma layer becomes thinner than the crust, where we enforce a minimum of 10 cells in the liquid magma layer. Owing to the large range of our parameter space (see Section 2.2) we always discuss our simulation resolutions in relative terms rather than absolute. We note that the standard, 5 km, resolutions used by Potter et al. (2012) also resulted in 10 cells in their 50 km crust. We provide a more detailed discussion of resolution and grid geometry in the supplementary material.

Our simulations are allowed to run until visible rippling in the surface has ceased and the hole diameter, as defined in Section 3.1, has reached a stable plateau. This can require quite long simulation times of up to several hours post-impact, adding to our computational considerations. The convergence of our simulations is discussed in more detail in the supplementary material. Full details of cell resolutions and simulation volumes, along with other metrics and initialisation files for our iSALE runs are included in our online Zenodo archive[1], with a summary provided in the supplementary material.

2.2 Parameter space

We simulate a total of 252 unique combinations of impactor diameter, impact velocity, and crust thickness (see Fig. 1), with a number of points simulated at multiple resolutions for convergence testing (see the supplementary material for more details). Our parameter space includes impactors with diameters ranging from 100 m to 30 km and crust thicknesses ranging from 1 to 40 km (corresponding to magma ocean depths between 98 and 11 km respectively). These crust thicknesses can be compared against the $\sim$45 km average thickness of the lunar crust today (e.g., Wieczorek et al. 2013).

To inform our impact velocity range, we utilise the same N-body simulation as P+18, which has the same initial conditions and setup as Jackson & Wyatt (2012), but a larger number of debris particles (10^5), and a longer integration time (100 Myr). From this simulation we find that 90% of impactors strike the Moon at less than 15 km/s, while 2/3 of impactors strike at less than 9 km/s. As such we use 15 km/s as our highest impact velocity and focus on the range <9 km/s. The lowest impact velocity is set by the escape velocity from the Moon and Earth at the lunar orbital distance. For the present day lunar

[1] https://doi.org/10.5281/zenodo.6824907

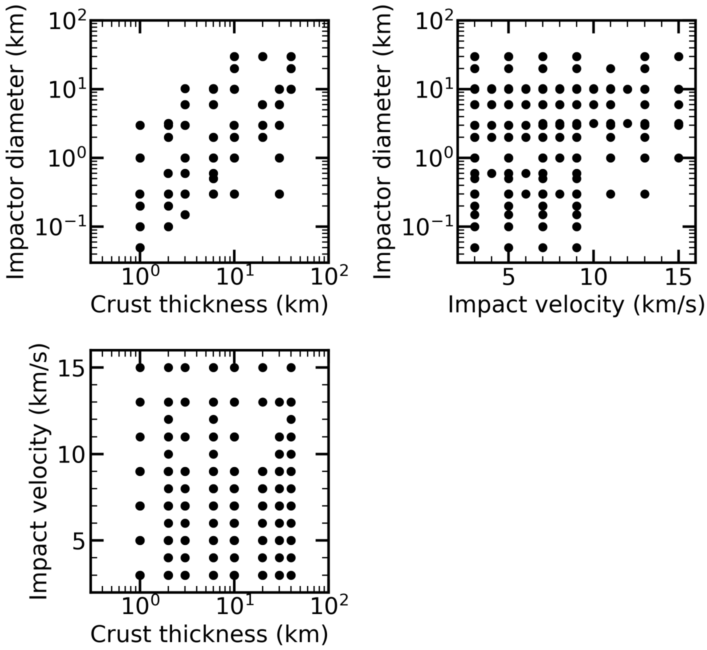

Figure 1. Graphical representation of the parameter space investigated in our suite of iSALE simulations showing each projection of the 3 dimensional space of impactor diameter, impact velocity, and crust thickness.

orbit the addition to the escape velocity from Earth is negligible, yielding a minimum impact velocity of ∼3 km/s, but early in lunar history the Moon was closer to Earth than it is today, increasing the minimum impact velocity. To cover all scenarios we set our minimum impact velocity as 3 km/s, but note that for a more typical early lunar separation of 10 Earth radii the minimum impact velocity would have been just over 4 km/s, due to the additional velocity gained from falling deeper into the gravity well of Earth.

As we are primarily interested in penetration of the crust and the boundary between cratering and penetration we do not simulate the smallest impactors striking the thickest crust or the largest impactors striking the thinnest crust. These would invariably lead to predictable end-member outcomes (cratering, or complete disruption/penetration of the crust), which as we demonstrate later, can be predicted by outlining the boundaries of the intermediate regimes.

3 Outcome morphologies

Our impact simulations result in a range of different final morphologies. Small, low-velocity impactors produce craters on the surface whereas larger and higher-velocity impactors breach the crust as a penetrating impact. Within both main categories we identify two sub-categories. In cratering impacts, crustal fracturing can be localised in a roughly hemispherical bowl centred on the impact site, which for want of a better term we call 'classical cratering.' Alternatively, the fracture zone can reach the base of the crust producing a more complex zone of fractured crust with a broadly cylindrical overall shape. We identify this sub-category as 'cratering with full-depth fracturing,' which in figure legends we will shorten to 'CFDF'.

Within the category of penetrating impacts, in less energetic impacts crustal material is able flow back in to close the hole after the crust has been breached, albeit the crust

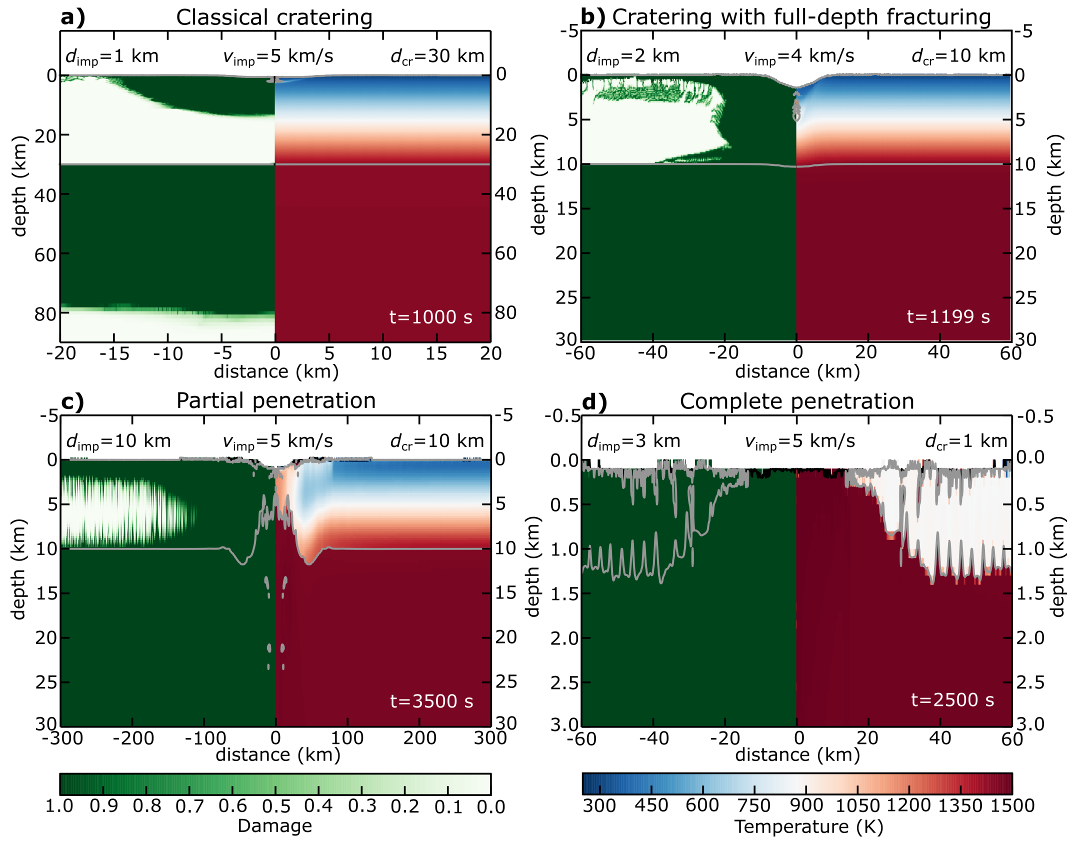

Figure 2. Examples of each category of outcome morphology. **a)** classical cratering. **b)** cratering with full-depth fracturing. **c)** partial penetration. **d)** complete penetration. Note that horizontal and vertical scales are not uniform across panels and aspect ratios are non-equal to emphasise the region of interest. Each panel is labelled with impactor diameter, d_{imp}, impact velocity, v_{imp}, crust thickness, d_{cr} and the simulation time at which the snapshot is taken, t. The crust material boundary is marked with a grey line. In each panel damage factor is shown on the left, while temperature field is shown on the right. A damage factor of 0 corresponds to fully intact, undamaged material, while a value of 1 corresponds to fully damaged material. The impact energies in each case are: a) 1.8×10^{19} J, b) 9×10^{19} J, c) 1.8×10^{22} J, d) 4.7×10^{20} J.

covering the impact zone is significantly thinner than the pre-impact crust. We term these impacts ‘partial penetration.’ At higher impact energies a wide enough initial hole is opened, and debris is substantially distributed elsewhere, such that return flow of material cannot completely close the hole. This leaves a central zone where the magma ocean is directly exposed to the surface after the simulation has settled. We term these impacts ‘complete penetration.’ Our main focus here is on penetrating impacts. We will typically refer to both cratering categories simply as ‘cratering.’

In Fig. 2 we show examples of each sub-categories of impact outcome, illustrating the different morphologies. In each panel we show damage factor on the left, where 0 corresponds to intact, undamaged material, and 1 corresponds to completely damaged material. The temperature field is shown on the right of each panel and the boundary of the crust is marked in grey. Note that in Fig. 2a, the surface expression of the crater is not visible due to the scale. As a strengthless liquid, the magma ocean is always completely ‘damaged’ in the simulation, but as noted above this does not have a physical meaning.

Between classical catering in Fig. 2a and cratering with full depth fracturing in Fig. 2b, in addition to the change in the region of damaged crust that defines the two sub-categories, we can also see that for larger craters relative to the crust thickness a bulge begins to appear at the base of the crust as a basal reflection of the surface crater.

When the impactor breaks through the crust in a partially penetrating impact, as shown in Fig. 2c, only a very broad, shallow depression is left at the surface in the crustal material that has flowed back into the hole. Instead the more dramatic topography occurs at the base of the crust, which appears much like an inverted version of a classical impact basin, with a relatively flat central ceiling and steep sides surrounded by a broad, thickened rim. The pattern of damage in the crust also changes relative to non-penetrating cases, now displaying a long sequence of alternating intact sections and fractures reflecting large scale flexure of the crust as it rides ripples induced in the magma ocean below.

For more energetic, complete penetration, impacts (see Fig. 2d) surface topographic variation is reduced even further as compared with Fig. 2c due to greater disruption of the crust and infill by magma. Below the surface a similar topographic profile to Fig. 2c is evident, with again steep sides and a flat ceiling, though here the ceiling thickness tapers to zero. In addition, the increased magnitude of ripples in the magma ocean now leaves an imprint in the structure of the crust itself with a series of partial tears. Animations of the two penetrating impacts shown in Figs. 2c-d are included as supplementary information to this manuscript.

Note that in our 2D, cylindrically symmetric geometry, we have only a single radial profile such that all structure seen in Fig. 2 is implicitly azimuthally symmetric. In a fully 3D simulation it is likely that this symmetry would be broken, with more complex fracture/block structures that include azimuthal variation. For the most part this is not an issue and we can treat the single radial profile as an approximate average profile, but there are a few instances where care must be taken in this, which we describe in more detail later.

3.1 Quantitative descriptions

To aid more quantitative analyses we begin with a simplified, diagrammatic representation of a complete penetration, shown in Fig. 3, in which we outline three concentric zones of interest with corresponding radii: 1) the central region within which the magma ocean is directly exposed to the surface, with radius R_{mag}, 2) the region in which the crust is thinned, with radius R_{thin}, and 3) the zone within which the majority of the crust is fractured, with radius R_{frac}. We use the following definitions for the three radii, which we found to be the most appropriate for our purposes in defining the size of the zones:

- R_{frac} is the radius at which the mean damage factor, $\bar{\Gamma}$, integrated vertically over a column of crust, drops below 0.5. This is designed to exclude the very broad zone of flexure fractures seen beyond 150 km in Fig. 2c
- R_{thin} is the radius at which crust thickness drops below 95% of its initial value. This captures well the largest extent of the region in which the crust has been thinned without being susceptible to numerical fluctuations.
- R_{mag} is the radius at which crust thickness drops to zero, however care is required regarding fragments of crust material that buoyantly rise into the cavity.

Returning to Fig. 2 we can see these zones appear progressively as we move from panels a-d, with none being present in panel a, while panel b possesses only a fracture zone, panel c shows a fracture zone and a zone of thinned crust, and in panel d all three zones are present.

From Fig. 3 and the definitions we can see that we will always have $R_{\mathrm{frac}} > R_{\mathrm{thin}} > R_{\mathrm{mag}}$. Our definitions do however involve a trade-off, in that the definition that works best for describing the size of a feature may not coincide with the one that is best for dividing different regimes. Our definition of R_{mag} corresponds to the transition between partial and

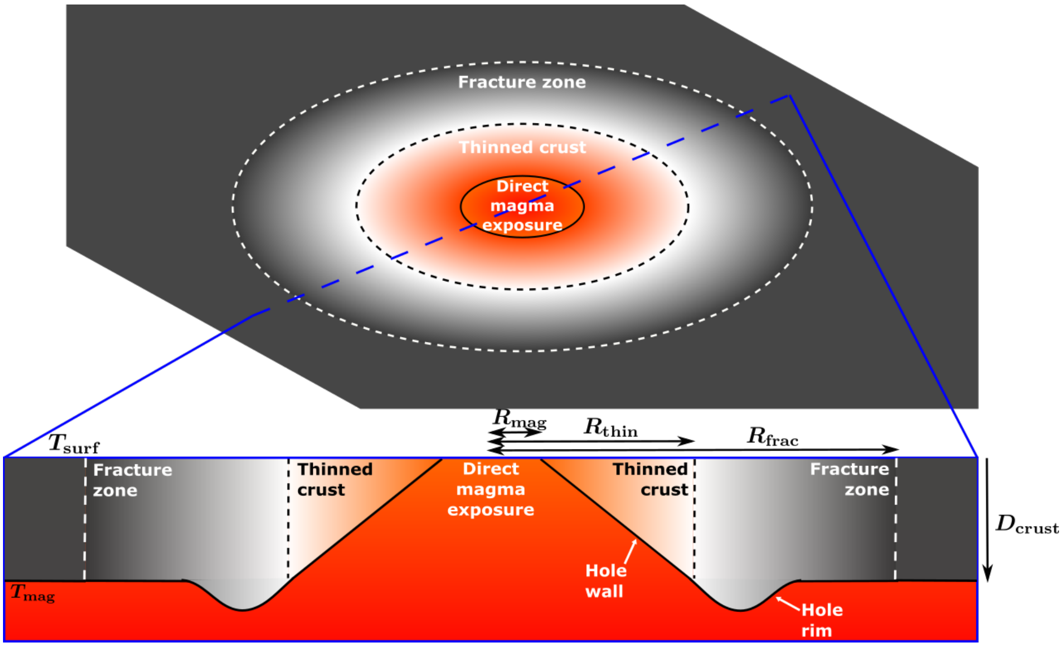

Figure 3. Diagram illustrating the different zones, direct magma exposure, thinned crust and fracture zone, for an impact that results in complete penetration.

complete penetration, with $R_{\mathrm{mag}} = 0$ marking the boundary, but this is not true for R_{frac} and R_{thin}. A large classical crater may have $\bar{\Gamma} < 0.5$ close to the centre and in both cratering regimes it is possible for more than 5% of the crust to be excavated at the centre. In these cases we found that it was better to separate the description of the regime transition from the definition of zone radius.

3.2 Transitions between the regimes

As described above, our definition for R_{mag} coincides with the partial – complete penetration transition with $R_{\mathrm{mag}} = 0$ for partial penetrations and $R_{\mathrm{mag}} > 0$ for complete penetrations. While this seems simple there is a potential complication in the form of 'rockbergs', fragments of crustal material floating in the magma within the central hole. These can result either from chunks calving off the inner rim of the annulus of thinned crust, or from pieces of crust that were pushed down into the magma buoyantly rising back into the hole. Such rockbergs appear in a number of our simulations, but their presence or absence is stochastic. The stochastic nature of these rockbergs encourages us that in a full 3D calculation they would be small, localised fragments that cover only a small fraction of the exposed magma area, rather than the circular annuli they technically represent in our 2D cylindrical simulations. As such we exclude any disconnected sections of crust from our calculation of R_{mag}.

Since our definition of R_{thin} does not mark the boundary between cratering and penetrating regimes we turn instead to the transient cavity formed during the initial stage of the impact. In Fig. 4 we plot maximum transient cavity depth in each simulations against crust thickness, with colour and point style differentiating outcome regimes, and a black line marking equality between the two quantities. Here we define transient cavity depth simply as the maximum depth of the surface below the original surface level at any given time after impact. The maximum transient cavity depth is then the greatest depth to which the surface is depressed below its original level.

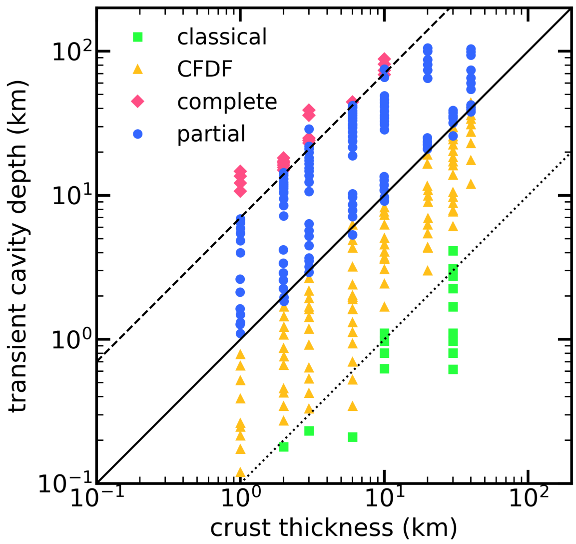

Figure 4. Comparison between crust thickness and maximum transient cavity depth, with different impact outcomes indicated by point colour. Equality between crust thickness and maximum transient cavity depth is shown by the solid black line while the dashed and dotted lines are factors of 7 above and 10 below respectively. CFDF is used as shorthand for Cratering with Full Depth Fracturing.

As we can see from Fig. 4, the solid black line marking equality between maximum transient cavity depth and crust thickness almost perfectly separates the cratering and penetrating regimes. There is a sharp change in material properties as we cross the base of the solid crust into liquid magma, so it is not surprising that there is a distinct transition in impact outcome corresponding to the point at which the transient cavity breaches the base of the crust. The maximum transient cavity depth is also a good predictor of the transitions from classical cratering to cratering with full depth fracturing, and partial to complete penetration, as shown by the dotted and dashed lines.

4 Scaling relations

We now examine the relationship between hole size and the impact parameters. Scaling relations for the size of impact craters have a long history (e.g., Nordyke, 1962; Gault, 1974; Holsapple & Schmidt, 1982), which we draw on in considering scaling relations for holes. We saw in Fig. 4 that transitions between regimes are well predicted by a constant ratio of transient cavity depth to crust thickness. The size of the transient cavity typically scales well with impact energy (e.g. Melosh, 1989) so in the left-hand panel of Fig. 5 we plot crust thickness against impact kinetic energy, marking the outcome regimes. This illustrates that transitions between each outcome regime are well described by a power law relationship between crust thickness and impact kinetic energy.

Fitting the impact energy at each transition in terms of crust thickness we obtain

$$E_{\mathrm{pp-cp}} = 2.20 \times 10^{9} d_{\mathrm{cr}}^{3.64}, \tag{1}$$

for the partial – complete penetration transition, where d_{cr} is the crust thickness,

$$E_{\mathrm{c-p}} = 1.18 \times 10^{6} d_{\mathrm{cr}}^{3.64}, \tag{2}$$

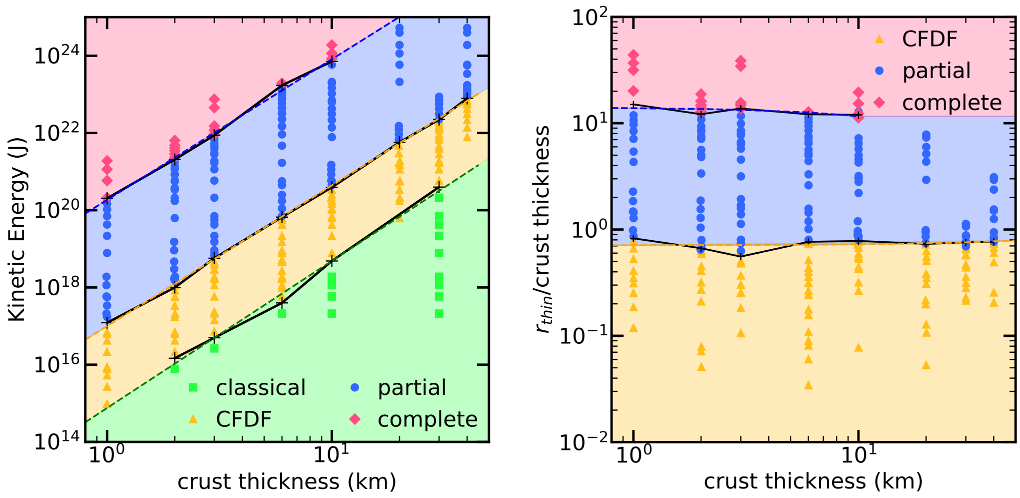

Figure 5. Divisions between outcome regimes in terms of kinetic energy and crust thickness (*left*), and crust thickness and ratio of hole radius to crust thickness (*right*). Points are coloured according to outcome regime, and regions corresponding to each regime are shaded in the same colour. The black lines connect points halfway between the pair of simulations lying either side of the transition between regimes for each crust thickness. The blue, orange, and green dashed lines are fits through the transition points for the partial-complete, cratering-penetrating, and classical-full-depth fracturing transitions respectively.

for the cratering – penetrating transition, and

$$E_{\mathrm{cc-cfdf}} = 3.46 \times 10^2 d_{\mathrm{cr}}^{3.81}, \tag{3}$$

for the classical – full-depth fracturing cratering transition (all quantities in mks SI units). The three transitions are marked in Fig. 5 as dashed blue, orange and green lines respectively. The cratering – penetrating and partial – complete penetration transitions are almost perfectly parallerl while the classical – full-depth fracturing transition appears slightly steeper but nonetheless still very close to parallel.

Additionally, in the right-hand panel of Fig. 5 we plot the ratio of R_{thin} to crust thickness, which shows that transitions between regimes occur at roughly constant values of this ratio.

4.1 Scaling of the partial penetration zone (R_{thin})

Since the regime transitions are well described by a power law relationship with impact kinetic energy we begin by examining the dependence of R_{thin} on impact kinetic energy in the left-hand panel of Fig. 6. We can clearly see that there is a strong correlation between R_{thin} and impact kinetic energy. However this correlation is modulated by crust thickness with points for each crust thickness lying in close to straight lines but offset from one another. As such we fit R_{thin} as a function of both impact kinetic energy and crust thickness of the form,

$$R_{\mathrm{thin}} = aE_{\mathrm{k}}^{b} d_{\mathrm{cr}}^{c}, \tag{4}$$

where E_{k} is impact kinetic energy and we find $a = 4.50 \times 10^{-3}$, $b = 0.385$, $c = -0.443$ with all quantities in mks SI units.

We show residuals for our fitted relationship in the right-hand panel of Fig. 6, which we compute as a ratio of the simulated value to the value predicted by the fitted relationship

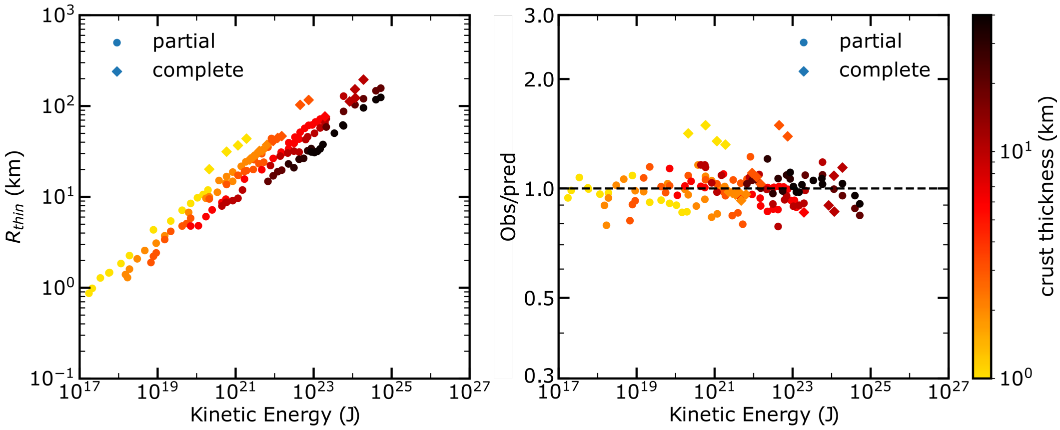

Figure 6. *Left*: R_{thin} as a function of impact kinetic energy. *Right*: Residuals (simulation value/fitted value) for our fit to R_{thin} as a function of impact kinetic energy and crust thickness. The dashed line marks equality between simulated and fitted value. In both panels points are coloured according to crust thickness while shape style shows partial and complete penetrations.

since ratios are more relevant to a power-law. The mean deviation between simulated and fitted values is 0.037 log units, or a factor of 1.09, so our fit is typically accurate to within 10%, while even the most deviant points are within 0.17 log units (a factor of 1.5). There are no clear trends in the residuals and while several of the most deviant points with residuals > 1 (i.e. underpredicted values) are complete penetrations the majority of complete penetrations lie within the same range as the partial penetrations. Substituting our relations for the kinetic energy at the transitions (Eqs. 1, 2) into Eq. 4 we find that at the boundary we should have $R_{\text{thin}} \propto d_{\text{cr}}^{0.96}$, matching the approximately constant ratio of R_{thin} to d_{cr} that we saw in Fig. 5.

4.2 Scaling of the exposed magma zone (R_{mag})

We saw in the right-hand panel of Fig. 5 that the transition from partial to complete penetration occurs at a roughly constant value of $R_{\text{thin}}/d_{\text{cr}}$, in this case $R_{\text{thin}}/d_{\text{cr}} \approx 13$. In addition, at the transition we have $R_{\text{mag}} = 0$ and above the transition R_{thin} continues to increase in the same way as below the transition. This suggests there is a limit to how much the crust surrounding the hole can be deformed and drawn back inwards following collapse of the transient cavity, at least without the inner edge fragmenting and forming rockbergs floating in a central magma pool rather than a continous ring of thinned crust.

Taking the mean of $(R_{\text{thin}} - R_{\text{mag}})/d_{\text{cr}}$ gives 12.6 with a mean deviation of 0.06 log units (a factor of 1.15) and a maximum deviation of 0.20 log units (a factor of 1.6). This suggests there is indeed a reasonably well defined relationship with the ring of thinned crust surrounding the central magma pool staying roughly constant in width for a given crust thickness.

We can also try more complex fits. Fitting a function of the form $(R_{\text{thin}} - R_{\text{mag}}) = a d_{\text{cr}}^{b}$ produces $a = 14.0$ and $b = 0.88$, slightly shallower than linear such that holes in thicker crust have proportionately slightly narrower rings of thinned crust around the edge. The mean log deviations with this fit are smaller at 0.051 log units, but the maximum deviation is larger at 0.21 log units. Trying a similar functional form to that we used for R_{thin} in Section 4.1, $R_{\text{mag}} = a E_{\text{k}}^{b} d_{\text{cr}}^{c}$ (for which we obtain $a = 1.07 \times 10^{-11}, b = 1.26, c = -3.74$) gives both worse mean and maximum log deviations, at 0.12 and 0.44 log units respectively.

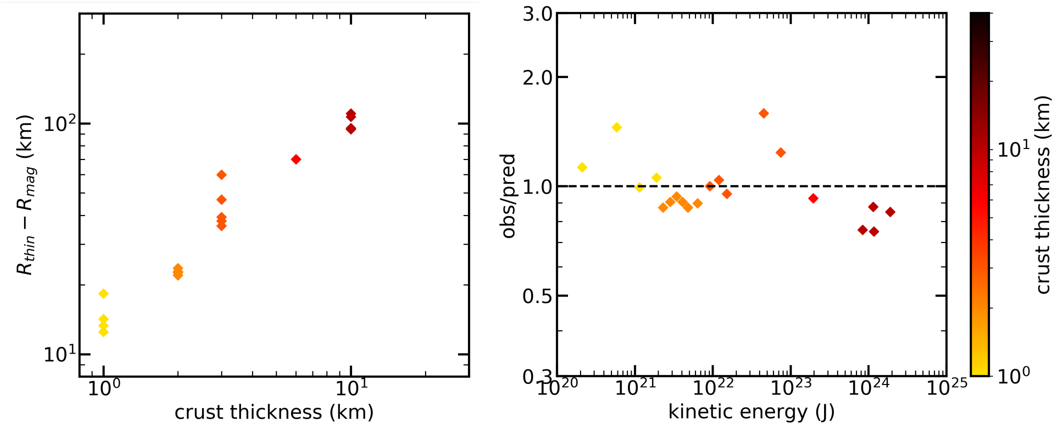

Figure 7. *Left*: $R_{\rm thin} - R_{\rm mag}$ as a function of crust thickness. *Right*: Residuals (simulation value/fitted value) for our fit to $R_{\rm thin} - R_{\rm mag}$, displayed relative to the impact kinetic energy. The dashed line marks equality between simulated and fitted value. In both panels points are coloured according to crust thickness.

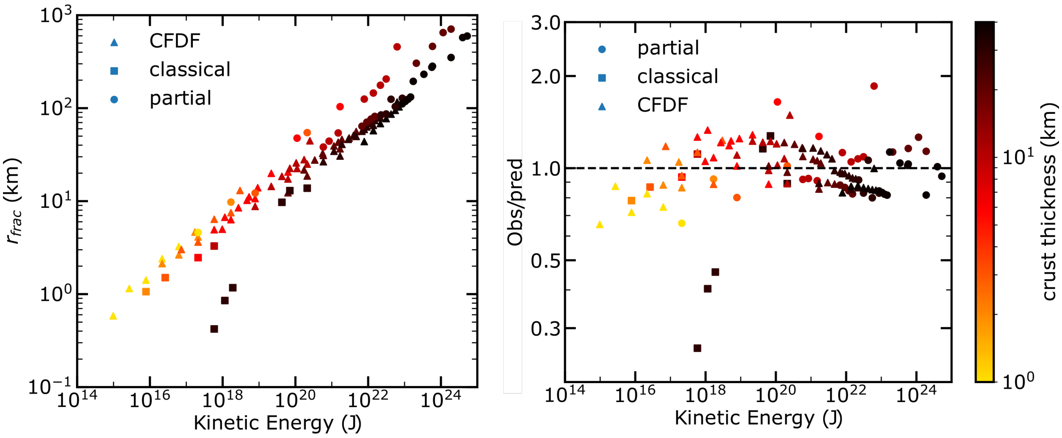

Figure 8. *Left*: $R_{\rm frac}$ as a function of impact kinetic energy. *Right*: Residuals (simulation value/fitted value) for our fit to $R_{\rm frac}$ as a function of impact kinetic energy and crust thickness. The dashed line marks equality between simulated and fitted value. In both panels points are coloured according to crust thickness, while point style indicates outcome regime.

Given the minimal improvement at best provided by more complex fits we favour the simple constant relationship,

$$R_{\rm mag} = R_{\rm thin} - a d_{\rm cr}, \tag{5}$$

where $a = 12.6$.

4.3 Scaling of the fracture zone ($R_{\rm frac}$)

In the left-hand panel of Fig. 8 we show $R_{\rm frac}$ relative to impact kinetic energy. As for $R_{\rm thin}$ previously, we see that there is a strong correlation between $R_{\rm thin}$ and impact kinetic energy, modulated by crust thickness. As such we fit $R_{\rm frac}$ in the same way as,

$$R_{\rm frac} = a E_{\rm k}^{b} d_{\rm cr}^{c}, \tag{6}$$

where we find $a = 0.0700$, $b = 0.382$, $c = -0.540$, with all quantities in mks SI units. Note that we do not include the classical cratering points in our fit since it is not clear if R_{frac} should obey the same scaling in cases where the fracture zone does not reach the base of the crust. In addition we exclude cases where R_{frac} >80% of the width of the high-resolution zone to avoid numerical artefacts.

Residuals for our fitted relationship are shown in the right-hand of Fig. 8, which as in Fig. 6 we show as a ratio of the simulated value to the value predicted by the fitted relationship. The mean deviation between simulated and fitted values is 0.062 log units, or a factor of 1.15, so our fit is typically accurate to within 15%, while the most deviant partial penetration or full-depth fracturing point is off by 0.27 log units (a factor of 1.9). There is some evidence of a trend in the residuals, with simulations around 10^{20} J being typically more underpredicted (residuals > 1) than those at lower or higher energies, which are more likely to be overpredicted (residuals < 1). We do not find an obvious additional variable that we could include to account for this however, and given the relatively small size of the residuals over 10 orders of magnitude in impact energy we consider the fit satisfactory.

The dependence on impact kinetic energy in Eqs. 6 and 4 is the same, while dependence on crust thickness differs only very slightly, with R_{frac} having a slightly stronger dependence on crust thickness. This slightly stronger dependence on crust thickness matches that found in Eq. 3 such that, as with R_{thin}, the value of $R_{\mathrm{frac}}/d_{\mathrm{cr}}$ at the transition is very close to constant ($R_{\mathrm{frac}} \propto d_{\mathrm{cr}}^{0.99}$). This also means the ratio between R_{frac} and R_{thin} is fairly constant, with a weak trend to lower values of $R_{\mathrm{frac}}/R_{\mathrm{thin}}$ for thicker crust and larger values for thinner crust.

4.4 Pi-scaling

A commonly used tool in fitting scaling relations for craters is the Pi-scaling formalism (e.g. Melosh, 1989) which recasts the problem in terms of dimensionless ratios. We investigated using a modified version of the Pi-formalism to fit scaling relations for holes, but found it does not perform as well as the relationships we fit in terms of impact energy and crust thickness. The root of the issue can be seen in the definition of π_2, $1.61gL/u^2$, where g is acceleration due to gravity, u is impact velocity, and L is a length scale relevant to the problem. For typical cratering impacts into uniform targets L is taken to be the impactor diameter, but here we have two length scales of relevance, impactor diameter and crust thickness and we found that neither provides a complete description of the scaling behaviour by itself. As a result we find that Pi-scaling does not provide as good a description of the outcomes of our crust penetrating impacts as our impact energy-based relations. Additional information is provided in the supplementary material for comparison with our fits in the sections above.

5 Discussion

5.1 Comparison with results for ice

As we noted in Section 1, the closest analogue in the modern day for the rock-magma ocean impacts we simulate are impacts into the ice shells of Europa or Enceladus. Just like the rock and magma ocean system we examine for the early Moon, Europa and Enceladus have a solid crust that floats on a liquid layer below, the difference being that the material in question is water/ice rather than rock/magma.

5.1.1 Impact simulations on Europa

In Fig. 9 we show the results of simulated impacts into the ice shell of Europa from Bray et al. (2014); Cox & Bauer (2015) (hereafter B+14 and CB15), overlaid on the regime transitions for our lunar rock-magma simulations. The CB15 dataset is the larger of the two and in addition to categorising impacts as penetrating or cratering they also identify

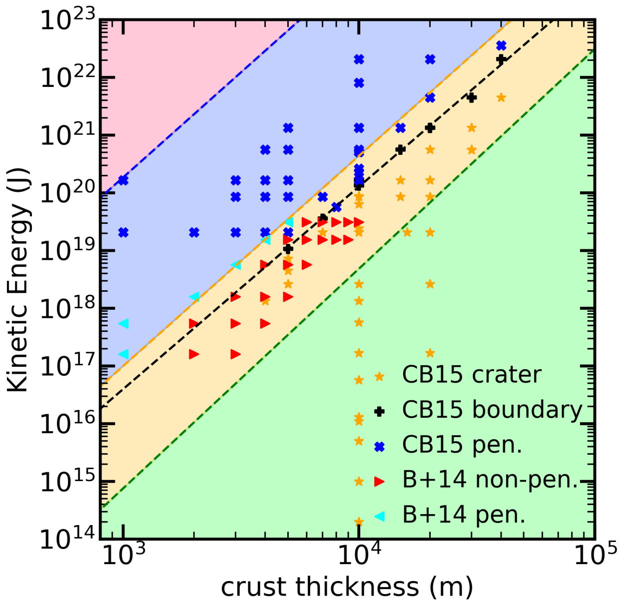

Figure 9. Comparison between the results of Bray et al. (2014)(B+14) and Cox & Bauer (2015)(CB15), who simulated impacts into the ice shell of Europa, and our regime transitions. The black dashed line is a fit to the cratering-penetrating boundary for the CB15 data. The shading follows Fig. 5: Pink = complete penetration, blue = partial penetration, orange = cratering with full-depth fracturing, green = classical cratering.

boundary cases. We perform a power-law fit to the boundary cases of CB15, which we show as the black dashed line in Fig. 9. This is roughly parallel to the cratering-penetrating boundary we determined for our lunar data, but a factor of 2-3 lower in impact energy. The B+14 data on the other hand is consistent with our cratering-penetrating boundary.

Both B+14 and CB15 used iSALE with essentially the same simulation setup and material parameters for their impact simulations. CB15, however define the transition between cratering and penetrating to occur when the maximum transient cavity depth reaches 90% of crust thickness, whereas B+14 define the transition to occur at equality between maximum transient cavity depth and crust thickness, as we do. This is likely the cause of the factor 2-3 difference in impact energy between the cratering-penetrating transition found by CB15 and that found by Bray et al. (2014) and our study.

Europa has roughly the same surface gravity as the Moon (1.314 m s^{-2} vs 1.62 m s^{-2}) and the simulations of B+14 and CB15 lie within the range of energies and crust thicknesses we used for our lunar rock-magma simulations. As such any differences between the results of our simulations and those of B+14 or CB15 should be due to differences in the material properties of rock-magma and ice-water, the most prominent being density, which is a factor of around 3 lower for ice-water. The similarity between the results of the three studies suggests there is little dependence on material properties. Confirming this lack of dependence on material properties is a clear avenue for future study.

5.1.2 Ice impact experiments

For rock-magma impacts obtaining experimental data would be extremely difficult, but for the ice-water system experimental data is much easier to obtain. Despite this,

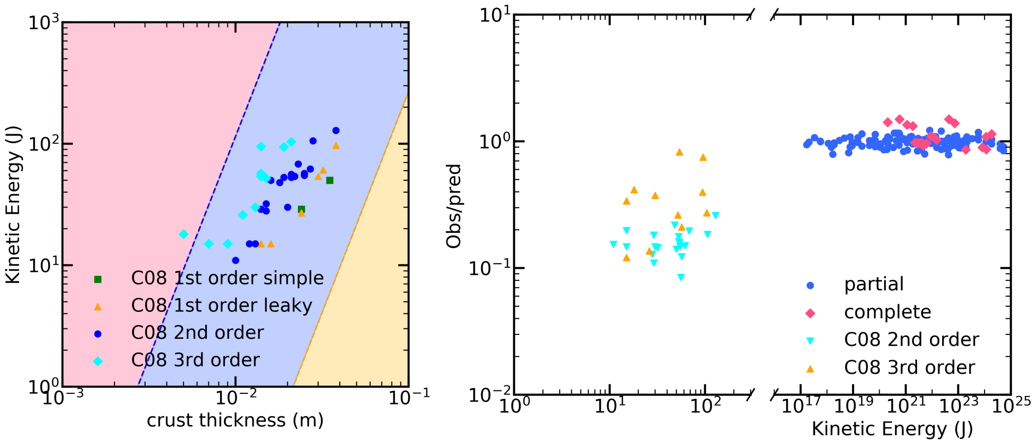

Figure 10. *Left*: Comparison between the experimental ice impact results of Cox et al. (2008) (C08) and our regime transitions. The shading follows Fig. 5: Pink = complete penetration, blue = partial penetration, orange = cratering with full-depth fracturing, green = classical cratering. *Right*: Residuals for our fit to R_{thin} including both our partially and completely penetrating simulations and the 2nd and 3rd order penetrating impacts from C08.

experimental data for impacts into ice over water are surprisingly sparse. The two most relevant studies are that of Cox et al. (2008) (hereafter C08), Harriss & Burchell (2017) (hereafter HB17), both of whom performed impact experiments into planar ice sheets overlying water. Harriss & Burchell (2020) also investigate ice/water targets, but in that work the targets are spheres roughly 20 cm in diameter, comparable to the size of the craters produced, which is a somewhat different scenario to the planar targets of our simulations and the other comparisons.

C08 divide their experimental results into three categories, which they term 1st order, 2nd order and 3rd order, which we show in Fig. 10. This three-fold division of outcomes does not neatly map onto our classification scheme, but we can make approximate analogies. Their 1st order impacts are described as craters, but include both 'simple' and 'leaky' craters, where C08 describe leaky craters as involving incipient penetration with cracks that allow liquid to bleed upwards into the crater. Six out of their eight 1st order impacts shown in Fig. 10 are leaky craters. With fractures that extend down to the base of the ice layer leaky craters seem comparable to our cratering with full-depth fracturing regime, while the simple craters match to our classical craters. We note however that the description in C08 leaves some ambiguity about whether the leaky crater class should be considered to overlap our partial penetration regime.

The 2nd and 3rd order outcomes in C08 are both clearly penetrating impacts, but 2nd order impacts have 'clean' holes with well-defined edges, while 3rd order impacts have more irregular holes with large ice rafts. We pair these outcomes roughly with partial and complete penetrations. In this case ice rafts in 3rd order outcomes are analogous to the large tears we saw in Fig. 2d, except that at this scale ice is not ductile and so the tears completely separate. The scattered nature of the ice rafts closest to the centre of the whole also provides further justification for ignoring rockbergs when determining the size of the exposed magma region earlier.

By comparison with our regime transitions we can see that the boundaries between different experimental outcomes for C08 appear slightly shallower, and are significantly closer together. Nonetheless, if we compare the boundary between 2nd and 3rd order with our partial-complete penetration transition, or the 1st order leaky and 2nd order boundary with our cratering-penetrating transition we see that the energies are within around an order of magnitude.

We can also compare our regime transitions with HB17, who performed 8 impact experiments with ice sheets overlying water. They varied ice layer thickness while keeping impact velocity in a narrow range of 4.89-5.38 km/s, corresponding to impact energies of 57-69 J with their 1.5 mm diameter aluminium projectiles. They found the transition from penetrative to non-penetrative impacts occurred for an ice thickness of 20 mm, roughly in the centre of the 2nd order impacts of C08 for this energy range, and similarly in the centre of our partial penetration regime. As with the results of C08, the transition energy of HB17 is within around an order of magnitude of our regime transition boundary.

For their experimental data, C08 also provides the hole size for 2nd and 3rd order outcomes, information that we do not have for the simulations of B+14 or CB15 above. This allows us to use Eq. 4 and compare our predicted hole size with the experimental result, which we do in the right-hand panel of Fig. 10. Our predicted hole sizes are about a factor of 5 too large, roughly matching the offset from the partial-complete transition in the left-hand panel of Fig. 10.

It is important to bear in mind that in comparing our results to the experimental data of C08, or HB17, we are extrapolating down by 5 orders of magnitude in size from km-scales to cm-scales, or around 15 orders of magnitude in impact energy. While rock and ice can behave in a ductile fashion at the energies and length-scales of our simulations, or those of B+14, CB15, ice is brittle at the much smaller energies and length-scales of the experimental data. In addition, while the simulations of B+14 and CB15 were performed in Europan gravity which is very similar to the lunar gravity of our simulations, the ice experiments were conducted on Earth, with gravity around 6 times higher. Considering this, that our predictions match the results of C08 to within a factor of around 5 is a surprisingly close agreement.

5.2 Comparison to work on lunar basins

While impact cratering during the very early stage of lunar evolution that interests us here has not previously been well studied, there have been many studies of basin formation at slightly later periods. Miljković et al. (2015)(hereafter M+15) performed simulations of lunar basin-forming impacts 3.5-4 Gyr ago. The temperature profiles they use as representative of the lunar nearside have a substantial layer below the crust that is close to or above the melting point due to concentration of radionuclide-rich KREEP material below the nearside crust. As such, their nearside simulations are quite similar to the impact simulations we performed in this study.

M+15 classify their simulations by whether or not mantle material is exposed in the basin centre at the end of the simulation, analogous to the distinction we make between partial and complete penetration. As we can see in the left-hand panel of Fig. 11 the partial-complete transition for our work matches well with the boundary between mantle exposure and no mantle exposure in M+15. M+15 also report the radius within which the crust is thinned, though it is not clear exactly how this radius is defined. In the right-hand panel of Fig. 11 we compare our predictions for R_{thin} from Eq. 4 with the results of M+15, and find that their results are consistent with our relationship, albeit with a slightly larger scatter.

We can also consider the specific case of South-Pole Aitken (SPA) basin, the oldest and largest definitive lunar impact structure. The formation of SPA was modelled by Potter et al. (2012) and while SPA does not have the concentration KREEP material that leads to the high sub-surface temperatures in the nearside simulations of M+15, the ancient age of SPA nonetheless implies a fairly hot interior. Potter et al. (2012) tested several different

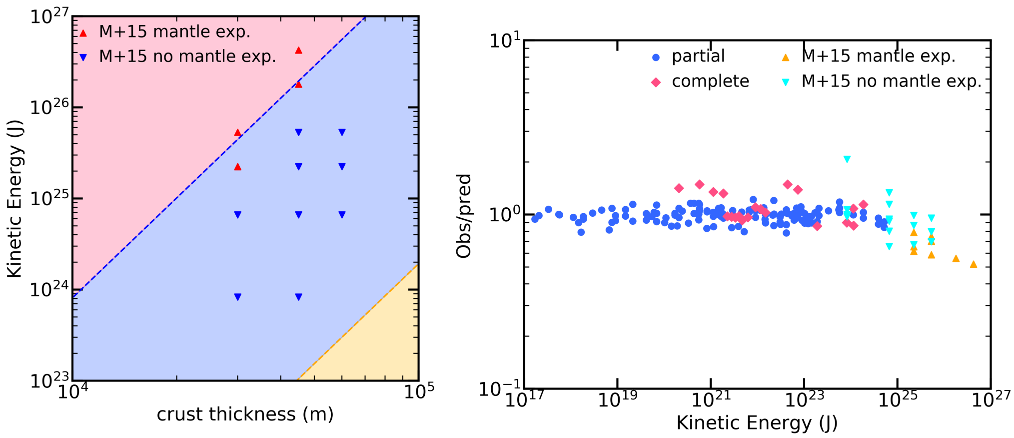

Figure 11. *Left*: Comparison between the lunar nearside impacts from Miljković et al. (2015)(hereafter M+15) and our regime transitions. Shading follows Fig. 5: Pink = complete penetration, blue = partial penetration. *Right*: Residuals for our fit to $R_{\rm thin}$ including both our partially and completely penetrating simulations and the results of M+15 for their nearside thermal profiles.

lithospheric temperature gradients, finding the steepest of these, 50 K/km, provides the best fit to SPA. This steep temperature profile is similar to those we use, except that we do not limit the temperature at the solidus. The best-fit simulation of Potter et al. (2012) uses an impact energy of 4×10^{26} J, with a 170 km diameter impacting striking at 10 km/s. This results in thinned crust within a radius of around 600-700 km and they note the innermost anorthosite (upper crust) at around 630 km. By comparison using our equation 4 with an impact energy of 4×10^{26} J and a crust thickness of 50 km yields a prediction of $R_{\rm thin}$=665 km, very similar to the results obtained by Potter et al. (2012).

5.3 Cooling of the lunar magma ocean

In Perera et al. (2018) (hereafter P+18) we examined how the solidification time of the LMO is modified by re-impacting debris penetrating the flotation crust. To do so we defined a parameter, k, the mass in impactors required per unit area of holes produced:

$$k \equiv \frac{M_{imp}(t_{step})}{A_{holes}(t_{step})}. \tag{7}$$

We then varied k across a wide range of values, keeping the value constant as a function of time. With the results of our impact simulations we can now examine what the value of this parameter should be.

A hole was defined by P+18 as exposure of the liquid magma ocean, such that for an individual impact we compute k as

$$k^{-1} = \frac{\pi R_{mag}^2}{m_{imp}}. \tag{8}$$

In Fig. 12 we show k computed in this way for our completely penetrating simulations - by definition k is infinite for simulations that do not result in complete penetration. Our simulations mostly lie at a lower value of k (more efficient hole opening) than the fiducial value of 10^7 used by P+18, with higher energy impacts having lower values of k than lower energy impacts. There is also a strong trend for increasing k with increasing crust thickness. Since crust thickness increases over time as the magma ocean solidifies this shows that a

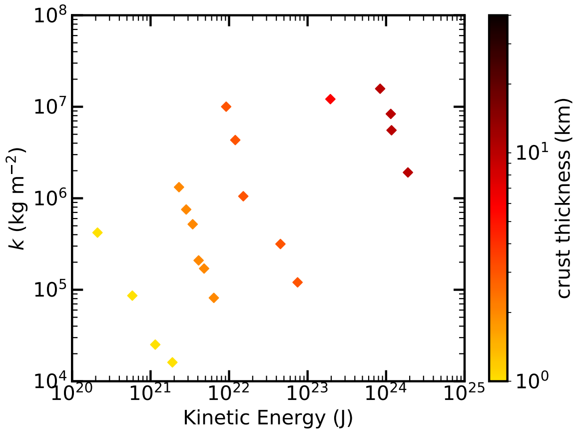

Figure 12. Impactor mass per unit area of exposed magma (k) as a function of impact kinetic energy and crust thickness.

k parameter that is constant in time is not a good assumption, instead k should vary over time.

We can also see this dependence of k on crust thickness by combining equation 8 with our equations for R_{mag} and R_{thin}, which yields

$$k^{-1} = \frac{\pi(R_{\mathrm{thin}} - 12.6d_{\mathrm{cr}})^2}{m_{\mathrm{imp}}} \tag{9}$$

$$= \frac{\pi}{m_{\mathrm{imp}}}\left(2.03 \times 10^{-5} E_{\mathrm{k}}^{0.77} d_{\mathrm{cr}}^{-0.886} - 0.113 E_{\mathrm{k}}^{0.385} d_{\mathrm{cr}}^{0.557} + 159 d_{\mathrm{cr}}^2\right). \tag{10}$$

We can clearly see the strong dependence on crust thickness, which means that a fairly typical impact involving a 10 km diameter impact striking at 10 km/s ($E_{\mathrm{k}} = 8.7 \times 10^{22}$) leads to $k = 3.2 \times 10^4$ for a crust thickness of 1 km, rising to $k = 5.5 \times 10^6$ at a crust thickness of 5 km, and shortly after that it ceases to penetrate.

While the values we find for k are typically lower than the fiducial value of 10^7 used by P+18, suggesting that the solidification time of the LMO is likely to be reduced, the strong dependence on crust thickness makes it clear that allowing k to vary with time is essential. Additionally, though P+18 only considered exposure of the magma ocean, there is a much larger area in which the crust is thinned, which would also allow faster heat loss, albeit not to the extent of direct magma exposure. The other important factor in P+18 is λ_{KE}, the fraction of the impactor kinetic energy that is converted into heat in the magma ocean. In a future study we will examine the kinetic energy conversion and incorporate effects into the magma ocean solidification scheme of P+18.

6 Conclusions

Immediately after formation, the Moon is expected to have been largely molten, with a deep, global Lunar Magma Ocean (LMO). The particular circumstances of the size and composition of the Moon lead to formation of an anorthositic flotation crust that is the precursor to the present lunar crust and which acts as an insulating blanket, slowing solidification of the LMO. At the same time however, the Moon would have experienced extensive bombardment over millions of years by returning debris that was released in the Moon-forming giant impact.

We have conducted a suite of impact simulations, spanning a range of impactor sizes, impact velocities, and crust thicknesses representative of this early bombardment of the Moon. We find that impact outcomes can be divided into two broad categories, cratering and penetrating, each of which can further be sub-divided into two, for four regimes in total: 'classical cratering,' 'cratering with full-depth fracturing,' 'partial penetration,' and 'complete penetration.' We also define three radii, $R_{\rm frac}$, $R_{\rm thin}$, and $R_{\rm mag}$, the radius of the fracture zone, the zone of thinned crust, and the central magma pool, respectively, which we use to describe the size of impact features.

The transitions between each regime are well described by power-law fits between impact energy and crust thickness, and are almost parallel. We find that $R_{\rm thin}$ and $R_{\rm frac}$ are both well described in terms of a power-law relationships with impact energy and crust thickness, of the form $aE_{\rm k}^{b}d_{\rm cr}^{c}$. The central magma pool in completely penetrating impacts is surrounded by a ring of thinned crust with a width roughly a constant multiple of the crust thickness, such that $R_{\rm mag}$ is well described by the simple relationship $R_{\rm mag} = R_{\rm thin} - 12.6d_{\rm cr}$.

We compare our results with previous work on penetration of the ice shells of Europa and Enceladus, finding an excellent match between our cratering-penetrating boundary and that for previous work on these bodies. Comparing with experimental data for ice yields surprisingly close agreement given the large extrapolations necessary. We also compare to previous work on the formation of early lunar basins, again finding close agreement with our cratering-penetrating boundary and predictions for $R_{\rm thin}$. Overall these comparisons suggest that our derived relations for the boundaries between different impact outcome regimes, and associated radii, are more broadly applicable than to just the rock-magma system of the very early Moon, with target density and material properties having relatively little influence on impact outcome. We intend to examine this further in future work.

Considering the work of Perera et al. (2018), we find that our simulated completely penetrating impacts are generally more efficient at exposing liquid magma than they assumed. This suggests that LMO solidication time should be decreased by more than the 34% they found for their fiducial assumptions. However, we also find that hole-opening efficiency is dependent on crust thickness, and thus on time. A complete comparison to Perera et al. (2018) thus also requires implementation of a time-varying hole-opening efficiency, which we will investigate in a future study.

Acknowledgements

This work was supported by NASA grant NNX16AI31G. T. S. J. Gabriel acknowledges fellowship support from the Arizona State University Space Technology and Science ("NewSpace") Initiative and from NASA grant 19-PLANET19R-0046. The authors gratefully acknowledge the developers of iSALE-2D, including Gareth Collins, Kai Wünnemann, Dirk Elbeshausen, Boris Ivanov, and Jay Melosh. The field of planetary science would not be where it is today without the contributions of Jay Melosh (1947–2020), and he will be greatly missed.

Data Availability

A Zenodo archive at https://doi.org/10.5281/zenodo.6824907 contains the following material:

- Table of all simulation parameters and derived data used in this manuscript, in machine readable CSV format
- Python scripts for generating all plots in this manuscript
- For all simulations, the initialisation file, a set of diagnostic plots, and a text file of derived data values
- Python scripts for processing the raw data and producing the diagnostic plots and derived data

The raw outputs of the iSALE simulations themselves are too large to be archived (over 1 TB of data), but the archived material is sufficient to allow any individual simulation to be exactly reproduced and processed, and to examine the outcome of any simulation in detail.

References

Agnor, C., & Asphaug, E. (2004, October). Accretion Efficiency during Planetary Collisions. *Astrophys. J. Lett.*, *613*, L157-L160. doi: 10.1086/425158

Amsden, A., Ruppel, H., & Hirt, C. (1980). *SALE: A simplified ALE computer program for fluid flow at all speeds* (Tech. Rep.). Los Alamos Scientific Lab., NM (USA).

Asphaug, E. (2014, May). Impact Origin of the Moon? *Annual Review of Earth and Planetary Sciences*, *42*, 551-578. doi: 10.1146/annurev-earth-050212-124057

Barr, A. C. (2016, September). On the origin of Earth's Moon. *Journal of Geophysical Research (Planets)*, *121*(9), 1573-1601. doi: 10.1002/2016JE005098

Bauer, A. W., & Cox, R. (2011, March). Hydrocode Modeling of Impacts at Europa. In *Lunar and planetary science conference* (Vol. 42, p. 1123).

Benz, W., Cameron, A. G. W., & Melosh, H. J. (1989, September). The origin of the moon and the single impact hypothesis. III. *Icarus*, *81*, 113-131. doi: 10.1016/0019-1035(89)90129-2

Benz, W., Slattery, W. L., & Cameron, A. G. W. (1988, June). Collisional stripping of Mercury's mantle. *Icarus*, *74*(3), 516-528. doi: 10.1016/0019-1035(88)90118-2

Bray, V. J., Collins, G. S., Morgan, J. V., Melosh, H. J., & Schenk, P. M. (2014, March). Hydrocode simulation of Ganymede and Europa cratering trends - How thick is Europa's crust? *Icarus*, *231*, 394-406. doi: 10.1016/j.icarus.2013.12.009

Cameron, A. G. W., & Ward, W. R. (1976, March). The Origin of the Moon. In *Lunar and planetary inst. technical report* (Vol. 7).

Canup, R. M. (2004, September). Dynamics of Lunar Formation. *Annu. Rev. Astron. Astrophys.*, *42*, 441-475. doi: 10.1146/annurev.astro.41.082201.113457

Canup, R. M. (2012, November). Forming a Moon with an Earth-like Composition via a Giant Impact. *Science*, *338*, 1052. doi: 10.1126/science.1226073

Canup, R. M. (2014, Aug). Lunar-forming impacts: processes and alternatives. *Philosophical Transactions of the Royal Society of London Series A*, *372*(2024), 20130175-20130175. doi: 10.1098/rsta.2013.0175

Collins, G. S., Melosh, H. J., & Ivanov, B. A. (2004). Modeling damage and deformation in impact simulations. *Meteoritics & Planetary Science*, *39*(2), 217–231. Retrieved from http://dx.doi.org/10.1111/j.1945-5100.2004.tb00337.x doi: 10.1111/j.1945-5100.2004.tb00337.x

Cox, R., & Bauer, A. W. (2015). Impact breaching of Europa's ice: Constraints from numerical modeling. *Journal of Geophysical Research: Planets*, *120*(10), 1708–1719. Retrieved from http://dx.doi.org/10.1002/2015JE004877 doi: 10.1002/2015JE004877

Cox, R., Ong, L. C. F., Arakawa, M., & Scheider, K. C. (2008, December). Impact penetration of Europa's ice crust as a mechanism for formation of chaos terrain. *Meteoritics Planet. Sci.*, *43*(12), 2027-2048. doi: 10.1111/j.1945-5100.2008.tb00659.x

Ćuk, M., & Stewart, S. T. (2012, November). Making the Moon from a Fast-Spinning Earth: A Giant Impact Followed by Resonant Despinning. *Science*, *338*, 1047. doi: 10.1126/science.1225542

Elbeshausen, D., Wünnemann, K., & Collins, G. S. (2009, December). Scaling of oblique impacts in frictional targets: Implications for crater size and formation mechanisms. *Icarus*, *204*, 716-731. doi: 10.1016/j.icarus.2009.07.018

Elkins-Tanton, L. T. (2012, May). Magma Oceans in the Inner Solar System. *Annual Review of Earth and Planetary Sciences*, *40*, 113-139. doi: 10.1146/annurev-earth-042711-105503

Elkins-Tanton, L. T., Burgess, S., & Yin, Q.-Z. (2011, April). The lunar magma ocean: Reconciling the solidification process with lunar petrology and geochronology. *Earth and Planetary Science Letters*, *304*, 326-336. doi: 10.1016/j.epsl.2011.02.004

Gabriel, T. S. J., Jackson, A. P., Asphaug, E., Reufer, A., Jutzi, M., & Benz, W. (2020, March). Gravity-dominated Collisions: A Model for the Largest Remnant Masses with Treatment for "Hit and Run" and Density Stratification. *Astrophys. J.*, *892*(1), 40. doi: 10.3847/1538-4357/ab528d

Gault, D. E. (1974, July). Impact cratering. In R. Greeley & P. H. Schultz (Eds.), *A primer in lunar geology* (p. 137-175).

Harriss, K. H., & Burchell, M. J. (2017, July). Hypervelocity impacts into ice-topped layered targets: Investigating the effects of ice crust thickness and subsurface density on crater morphology. *Meteoritics Planet. Sci.*, *52*(7), 1505-1522. doi: 10.1111/maps.12913

Harriss, K. H., & Burchell, M. J. (2020, June). Catastrophic Disruption of Hollow Ice Spheres. *Planet. Sci. J.*, *1*(1), 19. doi: 10.3847/PSJ/ab8f34

Hartmann, W. K., & Davis, D. R. (1975, April). Satellite-Sized Planetesimals and Lunar Origin. *Icarus*, *24*(4), 504-515. doi: 10.1016/0019-1035(75)90070-6

Holsapple, K. A., & Schmidt, R. M. (1982, March). On the scaling of crater dimensions. II - Impact processes. *J. Geophys. Res.*, *87*, 1849-1870. doi: 10.1029/JB087iB03p01849

Ivanov, B., Deniem, D., & Neukum, G. (1997). Implementation of dynamic strength models into 2D hydrocodes: Applications for atmospheric breakup and impact cratering. *International Journal of Impact Engineering*, *20*(1), 411–430. Retrieved from http://www.sciencedirect.com/science/article/pii/S0734743X97875112 (Hypervelocity Impact Proceedings of the 1996 Symposium) doi: 10.1016/S0734-743X(97)87511-2

Jackson, A. P., & Wyatt, M. C. (2012, September). Debris from terrestrial planet formation: the Moon-forming collision. *Mon. Not. R. Astron. Soc.*, *425*, 657-679. doi: 10.1111/j.1365-2966.2012.21546.x

Leinhardt, Z. M., & Richardson, D. C. (2005, May). Planetesimals to Protoplanets. I. Effect of Fragmentation on Terrestrial Planet Formation. *Astrophys. J.*, *625*(1), 427-440. doi: 10.1086/429402

Leinhardt, Z. M., & Stewart, S. T. (2012, January). Collisions between Gravity-dominated Bodies. I. Outcome Regimes and Scaling Laws. *Astrophys. J.*, *745*, 79. doi: 10.1088/0004-637X/745/1/79

Melosh, H. J. (1989). *Impact cratering : a geologic process* (No. 11). Oxford, UK: Oxford University Press.

Melosh, H. J. (2007, January). A hydrocode equation of state for SiO2. *Meteoritics and Planetary Science*, *42*(12), 2079-2098. doi: 10.1111/j.1945-5100.2007.tb01009.x

Melosh, H. J., Ryan, E. V., & Asphaug, E. (1992). Dynamic fragmentation in impacts: Hydrocode simulation of laboratory impacts. *Journal of Geophysical Research: Planets*, *97*(E9), 14735–14759. Retrieved from http://dx.doi.org/10.1029/92JE01632 doi: 10.1029/92JE01632

Miljkovic, K., Collins, G. S., Chapman, D. J., Patel, M. R., & Proud, W. (2012, March). High-velocity impacts in porous solar system materials. In M. L. Elert, W. T. Buttler, J. P. Borg, J. L. Jordan, & T. J. Vogler (Eds.), *American institute of physics conference series* (Vol. 1426, p. 871-874). doi: 10.1063/1.3686416

Miljković, K., Collins, G. S., Wieczorek, M. A., Johnson, B. C., Soderblom, J. M., Neumann, G. A., & Zuber, M. T. (2016). Subsurface morphology and scaling of lunar impact basins. *Journal of Geophysical Research: Planets*, *121*(9), 1695–1712. Retrieved from http://dx.doi.org/10.1002/2016JE005038 doi: 10.1002/2016JE005038

Miljković, K., Wieczorek, M. A., Collins, G. S., Solomon, S. C., Smith, D. E., & Zuber, M. T. (2015, January). Excavation of the lunar mantle by basin-forming impact events on the Moon. *Earth and Planetary Science Letters*, *409*, 243-251. doi: 10.1016/j.epsl.2014.10.041

Monteux, J., Collins, G., Tobie, G., & Choblet, G. (2016). Consequences of large impacts on Enceladus' core shape. *Icarus*, *264*, 300-310. Retrieved from https://

www.sciencedirect.com/science/article/pii/S0019103515004480 doi: https://doi.org/10.1016/j.icarus.2015.09.034

Nordyke, M. D. (1962, May). An Analysis of Cratering Data from Desert Alluvium. *J. Geophys. Res.*, *67*(5), 1965-1974. doi: 10.1029/JZ067i005p01965

Nyquist, L. E., Wiesmann, H., Bansal, B., Shih, C.-Y., Keith, J. E., & Harper, C. L. (1995, July). ^{146}Sm-^{142}Nd formation interval for the lunar mantle. *Geochim. Cosmochim. Acta*, *59*, 2817-2837. doi: 10.1016/0016-7037(95)00175-Y

Ohnaka, M. (1995, January). A shear failure strength law of rock in the brittle-plastic transition regime. *Geophys. Rev. Lett.*, *22*(1), 25-28. doi: 10.1029/94GL02791

Perera, V., Jackson, A. P., Elkins-Tanton, L. T., & Asphaug, E. (2018, May). Effect of Reimpacting Debris on the Solidification of the Lunar Magma Ocean. *Journal of Geophysical Research (Planets)*, *123*, 1168-1191. doi: 10.1029/2017JE005512

Pierazzo, E., Artemieva, N., Asphaug, E., Baldwin, E., Cazamias, J., Coker, R., . . . others (2008). Validation of numerical codes for impact and explosion cratering: Impacts on strengthless and metal targets. *Meteoritics & Planetary Science*, *43*(12), 1917–1938. Retrieved from http://dx.doi.org/10.1111/j.1945-5100.2008.tb00653.x doi: 10.1111/j.1945-5100.2008.tb00653.x

Pierazzo, E., & Melosh, H. J. (2000). Understanding Oblique Impacts from Experiments, Observations, and Modeling. *Annual Review of Earth and Planetary Sciences*, *28*, 141-167. doi: 10.1146/annurev.earth.28.1.141

Pierazzo, E., Vickery, A. M., & Melosh, H. J. (1997, June). A Reevaluation of Impact Melt Production. *Icarus*, *127*(2), 408-423. doi: 10.1006/icar.1997.5713

Potter, R. W. K., Collins, G. S., Kiefer, W. S., McGovern, P. J., & Kring, D. A. (2012, August). Constraining the size of the South Pole-Aitken basin impact. *Icarus*, *220*, 730-743. doi: 10.1016/j.icarus.2012.05.032

Rankenburg, K., Brandon, A. D., & Neal, C. R. (2006, June). Neodymium Isotope Evidence for a Chondritic Composition of the Moon. *Science*, *312*, 1369-1372. doi: 10.1126/science.1126114

Reufer, A., Meier, M. M. M., Benz, W., & Wieler, R. (2012, September). A hit-and-run giant impact scenario. *Icarus*, *221*, 296-299. doi: 10.1016/j.icarus.2012.07.021

Rufu, R., Aharonson, O., & Perets, H. B. (2017, January). A multiple-impact origin for the Moon. *Nature Geoscience*, *10*, 89-94. doi: 10.1038/ngeo2866

Shoemaker, E. M. (1962). Interpretation of lunar craters. In Z. Kopal (Ed.), *Physics and astronomy of the moon* (pp. 283–359). New York/London: Academic.

Solomon, S. C., & Longhi, J. (1977). Magma oceanography. I - Thermal evolution. In R. B. Merril (Ed.), *Lunar and planetary science conference proceedings* (Vol. 8, p. 583-599).

Spicuzza, M. J., Day, J. M. D., Taylor, L. A., & Valley, J. W. (2007, January). Oxygen isotope constraints on the origin and differentiation of the Moon. *Earth and Planetary Science Letters*, *253*, 254-265. doi: 10.1016/j.epsl.2006.10.030

Taylor, S. R., Taylor, G. J., & Taylor, L. A. (2006, December). The Moon: A Taylor perspective. *Geochim. Cosmochim. Acta*, *70*, 5904-5918. doi: 10.1016/j.gca.2006.06.262

Thompson, S. L. (1990, March). *Aneos analytic equations of state for shock physics codes input manual* (Tech. Rep. Nos. SAND-89-2951, ON:DE90010198). Albuquerque, NM, USA: Sandia Labs. Retrieved from https://www.osti.gov/biblio/6939284 doi: 10.2172/6939284

Thompson, S. L., & Lauson, H. S. (1974, March). *Improvements in the chart d radiation-hydrodynamic code iii: revised analytic equations of state* (Tech. Rep. Nos. SC-RR–71-0714). Albuquerque, NM, USA: Sandia Labs.

Trowbridge, A. J., Johnson, B. C., Freed, A. M., & Melosh, H. J. (2020, December). Why the lunar South Pole-Aitken Basin is not a mascon. *Icarus*, *352*, 113995. doi: 10.1016/j.icarus.2020.113995

Wieczorek, M. A., Neumann, G. A., Nimmo, F., Kiefer, W. S., Taylor, G. J., Melosh, H. J., . . . Zuber, M. T. (2013). The Crust of the Moon as Seen by GRAIL. *Science*, *339*(6120), 671–675. doi: 10.1126/science.1231530

Wood, J. A., Dickey, J. S., Jr., Marvin, U. B., & Powell, B. N. (1970). Lunar anorthosites and a geophysical model of the moon. *Geochimica et Cosmochimica Acta Supplement*, *1*, 965.

Zhang, J., Dauphas, N., Davis, A. M., Leya, I., & Fedkin, A. (2012, April). The proto-Earth as a significant source of lunar material. *Nature Geoscience*, *5*, 251-255. doi: 10.1038/ngeo1429

Zhu, M.-H., Wünnemann, K., & Artemieva, N. (2017, November). Effects of Moon's Thermal State on the Impact Basin Ejecta Distribution. *Geophys. Rev. Lett.*, *44*, 11. doi: 10.1002/2017GL075405